Research papers

# Superporous nanocarbon materials upcycled from polyethylene terephthalate waste for scalable energy storage

Arash Mirjalili [a], Bo Dong [b], Taner Zerrin [c], Amir-Ali Akhavi [c], Mustafa Kurban [d], Cengiz S. Ozkan [a,c,*], Mihrimah Ozkan [a,b,**]

[a] *Department of Chemistry, University of California, Riverside, 900 University Ave., Riverside, CA 92521, USA*
[b] *Department of Electrical and Computer Engineering, University of California, Riverside, 900 University Ave., Riverside, CA 92521, USA*
[c] *Mechanical Engineering Department, Materials Science and Engineering Program, University of California, Riverside, 900 University Ave., Riverside, CA 92521, USA*
[d] *Department of Electrical and Electronics Engineering, Kırşehir Ahi Evran University, 40100 Kırşehir, Turkey*

ARTICLE INFO

ABSTRACT

Plastic pollution is becoming a universal threat affecting wildlife, marines, the atmosphere, soil, and human wellbeing. The insufficient waste management traditions, along with a growth in the "throw-away" and "single-use" culture, exacerbate the problem. Meanwhile, the fast-growing energy storage industry, such as the lithium-ion battery (LIB), requires renewable resources to provide a steady and reliable production supply chain. This work introduces a scalable industrial mature route to transform polyethylene terephthalate (PET) plastic waste into a superporous activated carbon material for rechargeable LIBs. We characterized the analytical properties of the waste-derived carbon material and used it to develop LIB anodes. Then, we generated carbon-silicon composite anodes by impregnating silicon nanoparticles (SiNPs) into the superporous connected architecture network. We conducted density functional-based tight-binding (DFTB+) quantum chemical calculations to elucidate the binding interactions between PET and SiNPs. By implementing electrochemical impedance spectroscopy (EIS), galvanostatic intermittent titration technique (GITT), and differential capacity analysis (DCA), we investigated the root causes of the degradation mechanisms of the material. Finally, our techno-economical study highlights the merits of a sustainable approach for transferring waste materials into valuable products such as energy storage. This work can create further research and development for recycling plastic wastes towards scalable stationary battery storage with the benefits of environmental sustainability and circular economics.

## 1. Introduction

Plastic pollution is dangerous to many organisms globally, including humans. For instance, the air we breathe in can contain Nano- and micro-sized plastics resulting from the mechanical degradation of abandoned macroplastics. They are found in the atmosphere, aquatic and soil ecosystems, sediments, remote islands, and even biomass. The ongoing plastic pollution problem is because of the rapid production developments along with a rise in "single-use" (including masks and gloves due to the COVID-19 pandemic) and "throw-away" culture. Despite the rising concerns about plastic pollution and its potentially negative environmental impacts, the petrochemical industry is investing over $209 billion in manufacturing virgin plastics from natural gas [1].

At the same time, waste management infrastructure is falling behind in keeping a meaningful pace with the fast production and ever-rising consumption rates [2,3]. According to recent data, 6.3 billion tons of plastics were produced between 1950 and 2015, of which only 9 % were recycled, and the remaining were incinerated or discharged into the natural environment. The continuation of current trends will add 12,000 metric tons of plastic waste to the natural environment by 2050 [4]. Plastic pollutions in aqua is mainly mismanaged waste that accounts for 5 to 12 million tons of plastic leaking into our oceans each year [5–7]. Reports warn that nearly 3 million tons of microplastics enter the marine environment each year, and by 2050, the weight of plastic waste could "far exceed" that of fish in all oceans, making it "a planetary emergency" [8,58]. It is estimated that one-third of the globally produced plastics are

used for packaging. This portion is usually not recycled and can accumulate in landfills as waste [3]. Among plastics, a significant source of waste is linked to polyethylene terephthalate (PET), followed by high-density polyethylene (HDPE), low-density polyethylene (LDPE), and polypropylene (PP) [9]. In general, PET is a ubiquitous plastic used for textile, packaging, electronics, thin-film coatings, and engineering resins, and models show a 3.5 % increase in its production each year [10]. Because of additives, colorants, and fillers in the manufacturing process, PET cannot be renewed into the original precursor product but can be converted into other functional materials. The intrinsic properties of plastics make them a valuable resource, and the socio-economic advantages of their recycling are well documented [11–15]. As an example, activated carbons generated from organic waste materials such as plastics are very appealing due to their porous structure, high surface area, chemical and thermal stability, and good electronic conductivity [16,17]. Several efforts have been explored to recycle PET waste for energy storage applications. For instance, Sun et al. examined the powderized PET particles obtained through a solvothermal process and tested their application as an anode material in LIBs [18]. Półrolniczak et al. presented the fabrication of an activated hierarchical carbon substance from PET waste bottles and tested its behavior in a Li-Sulfur system [19]. Energy storage capability of an upcycled PET waste material obtained through a microwave radiation process was studied and supported by DFT calculations [20]. In a study by Kim and co-workers, waste PET was used as an additive for a pyrolyzed fuel oil-derived anode material with capacity and rate capability improvements [21]. Recently, we reported the upcycling of PET plastic waste into a high surface-area carbon microstructure with a direct application in electric double-layer supercapacitors [22]. The process includes three primary steps: (1) the dissolution of PET waste, (2) the formation of PET nanofibers, and (3) pyrolysis/carbonization to produce activated carbon (detailed in the Methods section).

Most commercial LIBs utilize high-quality and relatively expensive graphite for anode fabrication. However, the scope of this article is to demonstrate a scalable method for manufacturing plastic waste-derived activated carbon material with acceptable quality for ultra-low-cost LIBs for large-scale stationary energy storage. The composition of the activated carbon and electrochemical performance of the material promoted us to consider further modification of the carbon nanostructure by revising the manufacturing process. We optimized our heat treatment and carbonization methods, making the modified material better suited for LIBs. We found that the peak temperature of 750 °C for two hours was suitable to produce a material with relatively the highest specific capacity when assembled in a Li—C half-cell (Fig. 1a). According to

Fig. 1a, under a C/5 constant current constant voltage charging and discharging (C/5 CC-CV), the electrode sample indicated good stability with an initial specific capacity of 201.31 mAh g$^{-1}$. The cell showed 84 % capacity retention with a specific capacity of 169.13 mAh g$^{-1}$ at the end of the 50th cycle. To test the material's rate capability and electrochemical stability, we cycled the Li—C battery under 1C CC-CV for 1000 cycles (Fig. 1b). From the figure, the cell showed an initial specific capacity of 87.4 mAh g$^{-1}$ with a capacity retention of 98 % after 1000 cycles, which offers the material's excellent stability for long-term use.

As we will demonstrate later in the analytical characterization section, we assigned the performance to the highly porous carbon structure consisting of reduced graphene oxide (rGO) and amorphous carbon (aC). Next, we utilized the PET-derived carbon architecture as the hosting material for a Si-containing carbon anode to improve the overall energy density. PET electrospun fibers were used as the conductive carrier structure for the introduced silicon nanoparticles (SiNPs). Commercially available SiNPs were homogeneously distributed in a PET solution before generating ultra-thin PET fibers with embedded SiNPs (Si@PET). While we aimed to obtain a boost in energy density to achieve the fabrication of ultra-low-cost LIBs, we kept the Si loading below 10 wt% (wt%). Further note that high-quality porous Si as an anode material is more expensive than a graphite anode. By adding SiNPs into dissolved PET, the electrospinning process resulted in an average of 8.77 wt% of Si in the anode, corresponding to a loading factor of 0.51 mg cm$^{-2}$ for our half-cells (please see the supporting information for details). Density Functional Based Tight Binding (DFTB+) calculations indicate close interactions between PET and SiNPs via active binding sites in PET. After electrospinning, the fibers were carbonized, and the obtained material (Si@C) was tested as an active anode material in a LIB half-cell.

## 2. Results and discussion

### 2.1. Analytical characterization & DFTB+ computations

The microstructure of Si@PET (Fig. 2a) and Si@C (Fig. 2b) was studied using scanning electron microscopy (SEM), Raman spectroscopy, and X-ray diffraction (XRD). From the SEM images shown in Fig. 2c-d, SiNPs are homogeneously distributed and surrounded by the fabric of very thin, smooth, and relatively uniform PET fibers, with diameter values ranging between 0.47 and 1.01 μm with a mean value of 0.76 μm (Table S2). We also noticed some Si agglomeration with a relative diameter of ~1–6 μm, as shown in Fig. S3. We conducted DFTB+ calculations to explore the interactions between PET and SiNPs within the silicon particle size range (R) of 0.7 nm (71 Si atoms) to 1.6
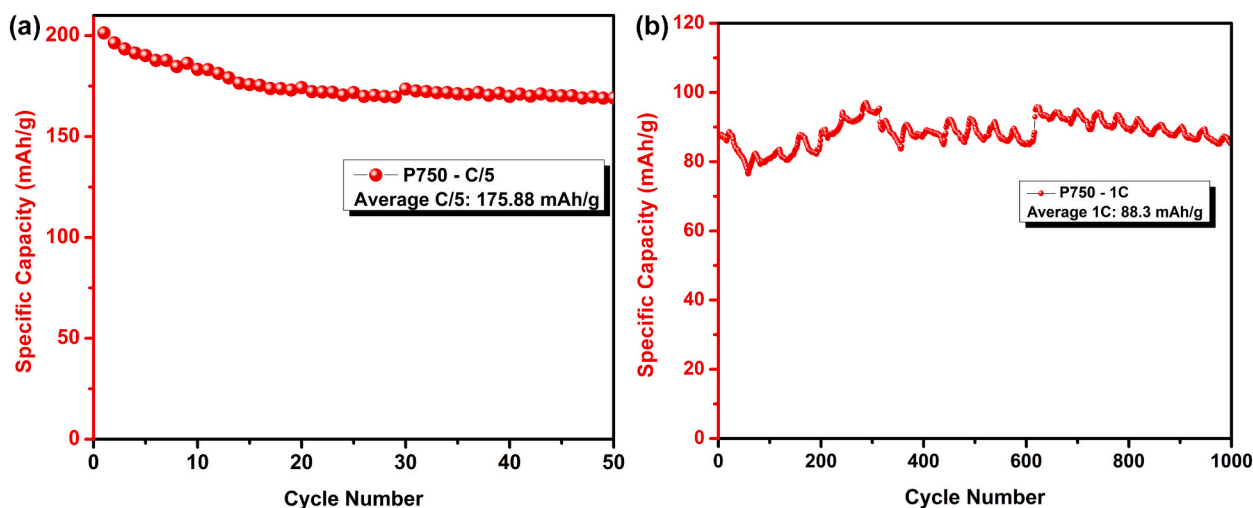


**Fig. 1.** (a) Cycling data of P750 at charge/discharge rate of C/5, and (b) longevity test of P750 at 1C for 1000 cycles. The material showed excellent stability, delivering 85.33 mAh g$^{-1}$ at the 1000th cycle with 98 % capacity retention.
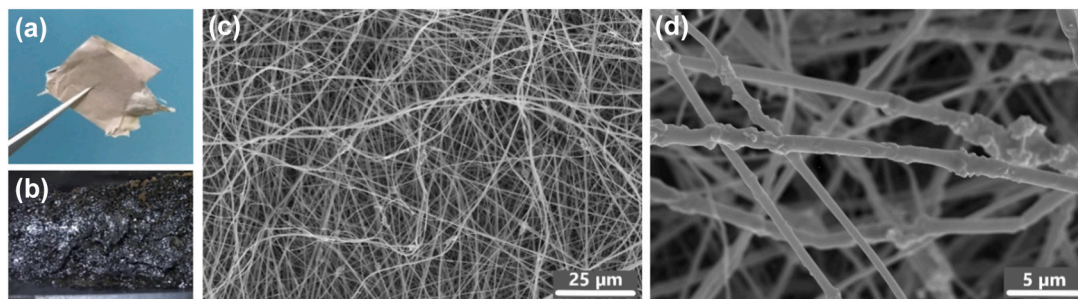
**Fig. 2.** Images of (a) an electrospun film (Si@PET) and (b) pyrolyzed sample (Si@C) in a quartz boat after carbonization. SEM images of Si@PET magnified to (c) 1000× and (d) 5000×. The development of a compressed forest of PET fibers enclosing Si particles, including some bulk Si clusters, is observed.

nm (849 Si atoms). DFTB+ is an approximation to the density functional theory (DFT) based on quantum mechanical modeling to investigate the structure of many-body systems and condensed phases. In order to understand the interactions better, we systematically considered several initial adsorption configurations and selected the most stable and optimized designs to further investigate the bindings between PET molecules and SiNPs. Since the primary focus of this part of the work is not to examine the variances among different bonding configurations, we only evaluated the optimized geometrical models with the most stable binding points for PET-SiNPs.

The binding energies of each corresponding case are provided in Table.S1. The binding energy of 6.8889 eV for PET+SiNP (for $R = 1.2$ nm) in Fig. 3 shows that the PET molecule binds strongly to the NP-R6 surface site, which indicates a stronger binding affinity compared to adsorptions on other NP models and just slightly more than the PET+SiNP adsorption for 6.8743 eV for $R = 1.0$ nm (see Fig. S2, Table S1). This means that SiNP with $R = 1.2$ nm can be more effective in attracting PET molecules than other SiNP models. Our benchmarks show that the most stable structure was obtained from interactions among two Si and two O atoms. Two O atoms of a PET molecule are inclined at an angle of 122.0° to the two Si atoms of SiNP (for R = 1.2 nm) surface, where bond lengths between Si and O atoms are found to be 1.972 and 1.850 Å (Fig. 2). On the other hand, binding energies from the interaction of PET molecules and Si as a function of SiNP size follow a considerably increasing trend from 3.9467 to 6.8889 eV with an increase of the SiNP size in the range from 0.7 (71 atoms) nm to 1.2 nm

(357 atoms), except for the case of 1.1 nm (5.6090 eV). When the SiNP size gets larger, there is a decreasing trend from 6.8889 eV (1.2 nm) to 3.8439 eV (1.4 nm). And moving from 1.4 nm to 1.6 nm, the binding energy remains nearly constant. For all models, the bond lengths between O atoms of PET and Si atoms of SiNPs change in the range of 1.80–1.97 Å.

Based on our DFTB+ calculations and because of the close interactions between PET molecules and SiNPs, while PET molecules surround the SiNPs, a homogeneous distribution of the particles could achieve. Moreover, this affinity which resulted in encapsulated SiNPs in a carbon supporting frame, could enhance Si electronic conductivity and help with the electrochemical performance of the LIB. Subsequently, we carbonized the electrospun fibers to generate a conductive carbon network and break down the organic linkers. Using Raman spectroscopy, we investigated the structural variation of Si@PET and Si@C samples plus the degree of graphitization and defect density of the supporting carbon frame [23]. The Raman spectrum of Si@PET (Fig. 4a) is an excellent match to the Raman spectra of untreated PET [24,25] with the addition of the following peaks: (1) a pronounced peak centered at 518.71 $cm^{-1}$, and (2) a broad peak near 960 $cm^{-1}$, corresponding to the first and second-order scattering of crystalline SiNPs, respectively; (3) the peak near 1069 $cm^{-1}$ is related to the vibrations of oxidized SiNPs (Si—O) [26].

This observation suggests a mild dissolution of PET plastic in the solvent environment. By rapid penetration of the solvent molecules into the chains of PET polymer, its structure would expand, allowing the
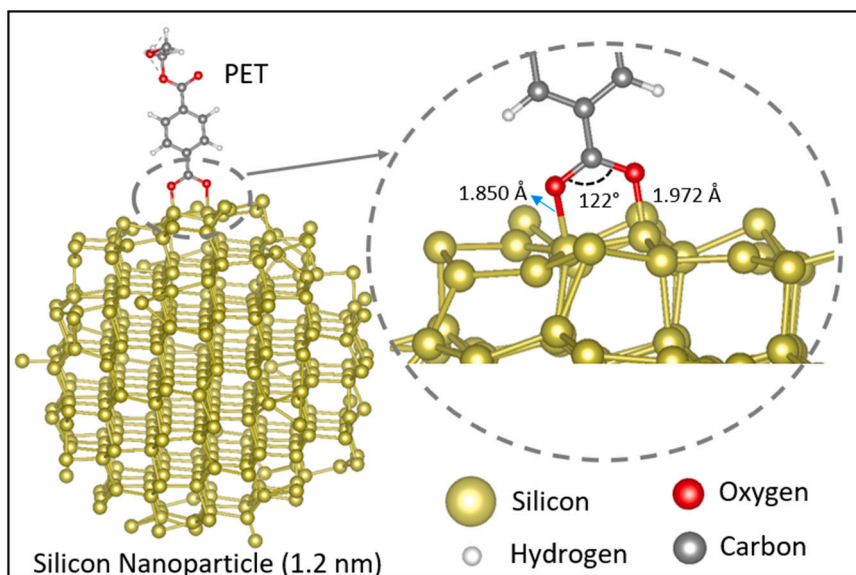


**Fig. 3.** The optimized geometry of interactions between PET and SiNPs (1.2 nm). The most stable structure was observed when 2 O atoms of PET interacted with 2 Si atoms at an angle of 122°. The bond length variation was found to be very similar for all the tested conformations.
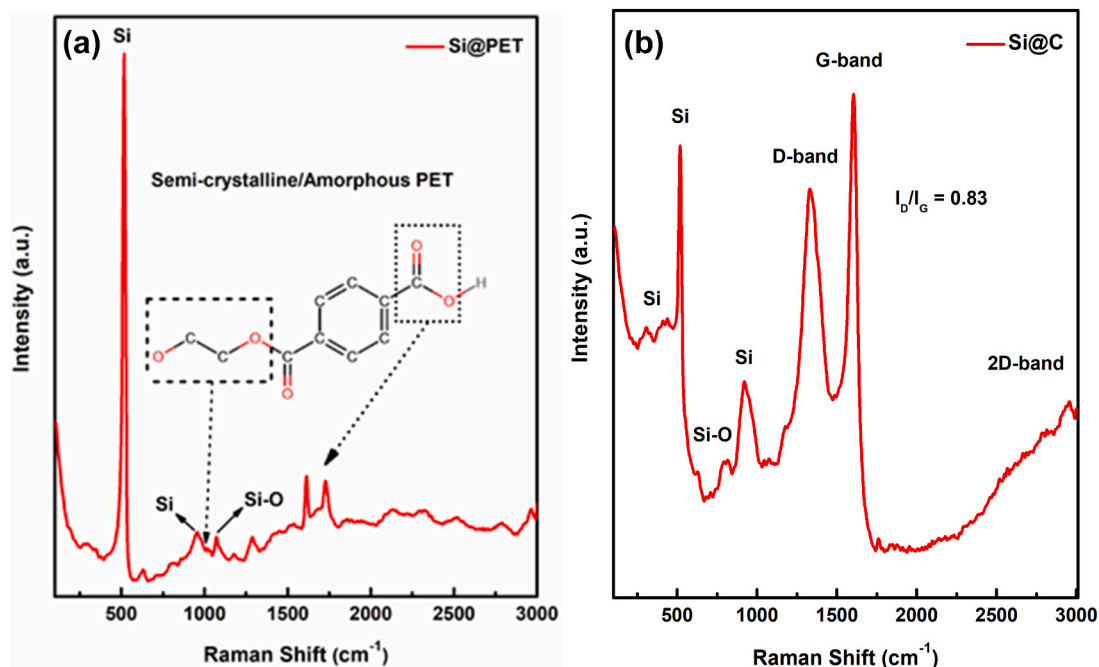
**Fig. 4.** Raman spectra of the (a) electrospun PET fibers enclosing Si nanoparticles indicate the presence of semi-crystalline/amorphous PET along with Si and silicon oxide peaks; Raman spectra suggest solvent-free PET fibers with SiNP addition (b) milled carbonized sample, exhibiting Si, silicon oxide, amorphous carbon, and rGO characteristics. Silicon oxide peaks are related to the formation of partially oxidized SiNPs upon contact with air and during the carbonization steps.

SiNPs to embed within the fibers. Raman spectra of the carbonized sample (Fig. 4b) consist of Si, silicon oxide, and carbon peaks. The peaks at 304.69 cm$^{-1}$ and 434.74 cm$^{-1}$ are related to the second-order acoustic phonon modes of bulk Si, representing the Si-XII and Si-III phases, respectively [27]. The observed peaks at 520.98 cm$^{-1}$ and 929.31 cm$^{-1}$ are characteristic of Si, and they are attributed to the first- and second-order scattering of polycrystalline SiNPs, respectively [28]. The shoulder peak at 802.75 cm$^{-1}$ is ascribed to oxidized SiNPs (Si—O), associated with silica intrinsic vibrational modes [29]. The peak at 1339.75 cm$^{-1}$, commonly referred to as the D-band, is related to the defects and disordered graphite, and it is a result of out-of-plane vibrations of carbon atoms with dangling bonds [30]. The peak at 1601.42 cm$^{-1}$ (the G-band) corresponds to highly ordered carbon

domains in a 2D hexagonal lattice which are sp$^2$ bonded (aromatic bonding and graphene structure). The broad peak starting at ~2500 cm$^{-1}$ with local peaks centered at 2842.23 cm$^{-1}$ and 2961.46 cm$^{-1}$ is the 2D band. This peak, the secondary D peak, is typically observed in carbon compositions consisting of rGO. Because it is susceptible to the stacking order of graphene layers (mono, double, or multi-layer), it can address the conformation of graphene sheets [31]. In general, mono-layer graphene has a pronounced peak centered at ~2679 cm$^{-1}$, but the intensity declines, and it becomes broadened with an increase in the number of graphene layers [32]. In this regard, considering the relatively low intensity and location of the peaks, we concluded that Si@C should contain some degree of multi-layer rGO.

The relatively high $I_D/I_G$ ratio of 0.83 suggests high disorder and low
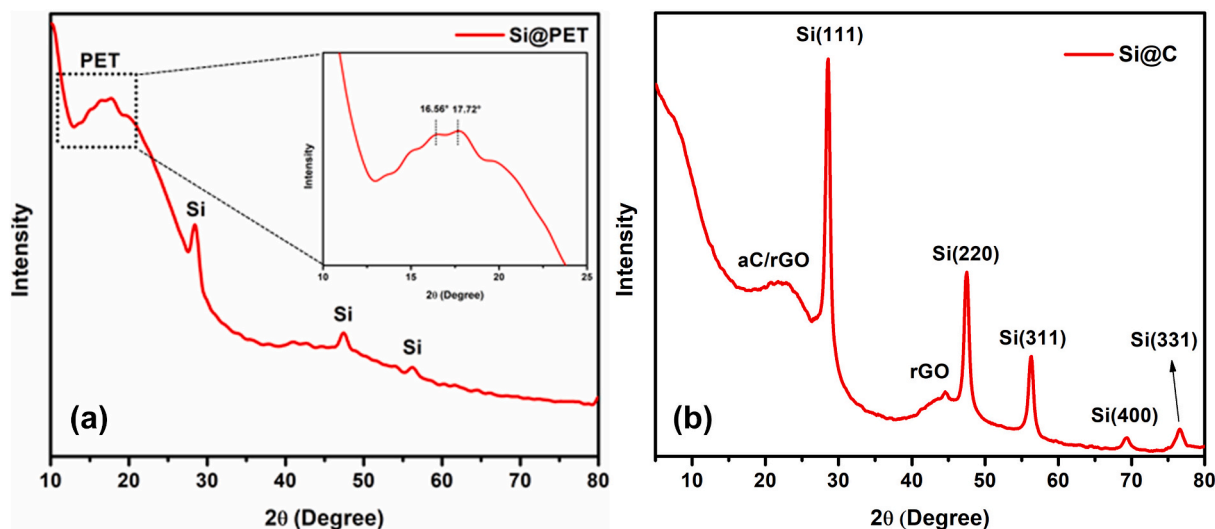


**Fig. 5.** XRD profiles of (a) electrospun fibers, confirming the existence of mixed semi-crystalline and amorphous structure of PET along with Si characteristic peaks. The relatively low intensity of silicon peaks can be due to the coverage with PET fibers; and (b) milled carbonized sample, showing the presence of amorphous carbon (aC), rGO, and silicon.

crystallinity degree of the Si@C and is also consistent with reports on rGO [33]. Fig. 5 displays the Si@PET and Si@C XRD patterns. From Fig. 5a, the peaks centered at 16.56° and 17.72° are characteristic of PET, and they are assigned to (011) and (010) planes, respectively [34]. Since fully amorphous PET exhibits a broad peak around 20°, we determined that the fibers have both amorphous and semi-crystalline regions while the amorphous zone is predominant [35]. Furthermore, the peaks at 28.37°, 47.74°, and 56.28° correspond to SiNPs. The relatively low intensity of Si peaks can imply that the surface chemistry is mostly Si-free. The position of the first peak and its relative interlayer spacing of 4.08 Å is suggestive of adequate reduction of the graphene oxide sheets. The supporting frame's mixed amorphous/graphitic structure is inherited from PET with an amorphous/semi-crystalline system discussed above. The peaks at 28.54°, 47.48°, 56.31°, 69.38°, and 76.56° are characteristic of crystalline SiNPs [36].

Sharp and narrow Si peaks suggest high crystallinity degrees for the particles, and they can be assigned to cubic phases of Si. This conclusion is in good agreement with our Raman spectral analysis, in which it was outlined that crystalline SiNPs are embedded in a mixture of amorphous and graphitic carbon networks. Fig. 6 displays the $N_2$ adsorption/desorption isotherms and relative pore volume distribution of Si@C. Brunauer-Emmett-Teller (BET) material analysis identified a microporous carbon network with a surface area and pore size of 400.1 m$^2$ g$^{-1}$ and 4.65 Å, respectively. The close distribution of the pore sizes (concentrating at 5.90 Å) can be suggestive of uniformly carbonized fibers that are relatively similar in their pore structure. Compared to our BET survey of carbonized PET fibers [22], the great match of details implies that the surface chemistry is not affected by the SiNP addition. The SEM image of Si@C and its analogous Energy-Dispersive X-ray Spectroscopy (EDS) mapping and the relative individual elemental profiles are shown in Fig. 7. The EDS data shows contributions from carbon (majority), silicon, and oxygen (minority). rGO is heavily contributing to the oxygen content in addition to a trace amount of silica.

## 2.2. Electrochemical characterization

A Cyclic Voltammetry (CV) plot of Si@C is shown in Fig. 8a. The CV curves display ordinary redox properties of Si with lithiation occurring at potentials below 0.3 V and delithiation at 0.40 V and 0.55 V [36,37]. The increase in the magnitude of anodic peaks with cycling is due to the continuous activation of the material that can undergo alloying with Li [38]. It has been reported that these two anodic peaks at 0.39 V and 0.55 V are attributed to amorphous Si, and further, they usually

represent the decomposition of the highest lithiated phase $Li_{4.2}Si$ and the complete delithiation of the Si electrode. The broad cathodic peak emerging during the first cycle (~0.1–0.7 V), which later disappeared with further cycling, is ascribed to the irreversible reactions due to Solid Electrolyte Interface (SEI) layer formation [39]. The peaks centered at ~0.16 V are related to the dealloying phase of $Li_xSi$ [40], and considering the relative gradual intensity increase with further cycling, it can infer farther dealloying with cycles which is directly related to the progressive activation of the electrode's material. No apparent shape variation was observed after the 7th cycle, suggesting that the Li intercalation and extraction reactions are stable during the charge/discharge cycles. The CV curve of the carbon frame is provided in the supporting information (Fig. S4). The potential profile of the investigated anode is displayed in Fig. 8b, where it shows a voltage range of 0–0.3 V during charging, associated with Li alloying, and 0.3–0.7 V during discharging, corresponding to Li dealloying. This finding is in good agreement with our CV analysis. For material activation and construction of a systematic SEI layer, the cells were conditioned for four cycles at C/50 (Fig. S5-a). The specific capacity and CE of the first cycle were equal to 239 mAh g$^{-1}$ and 38 %, respectively. At the end of the fourth cycle, the cell's capacity was promoted to 308 mAh g$^{-1}$ with a CE of 94 % (Fig. S5-b). The relatively low initial capacity and CE are referenced to irreversible SEI formation [41]. In this regard, the gradual increase in the capacity along with an enhancement in CE is proof of the activation step and near completion of the SEI formation. This ongoing activation is due to further penetration of the electrolyte into the mostly amorphous structure of the carbon network, accompanied by continuous Li alloying of newly accessible active sites [42].

Data on Galvanostatic Cycling with Potential Limitations (GCPL) is shown in Fig. 8c, which demonstrates the performance of the Si@C composite anode with a relatively gradual increase in capacity up to the 20th cycle. The cell delivered a capacity of 250 mAh g$^{-1}$ after 20 cycles, equal to 97 % of the initial value at the same C-rate. The Si@C electrode could deliver a reversible capacity of 163 mAh g$^{-1}$ after 150 cycles with a CE of 98.59 %. (The gravimetric capacity analyses were based on the total mass of the electrode, C, and Si loadings). The electronic conductivity of SiNPs is enhanced via immediate connections with the carbon atoms, enabling them to participate in the redox reactions. In general, understanding the degradation mechanism and the root causes of LIB systems can provide significant insights into the material modification, electrode development, and the battery's state of health estimation. In this respect, electrochemical characterization techniques of electrochemical impedance spectroscopy (EIS), galvanostatic intermittent titration technique (GITT), and differential capacity measurements were
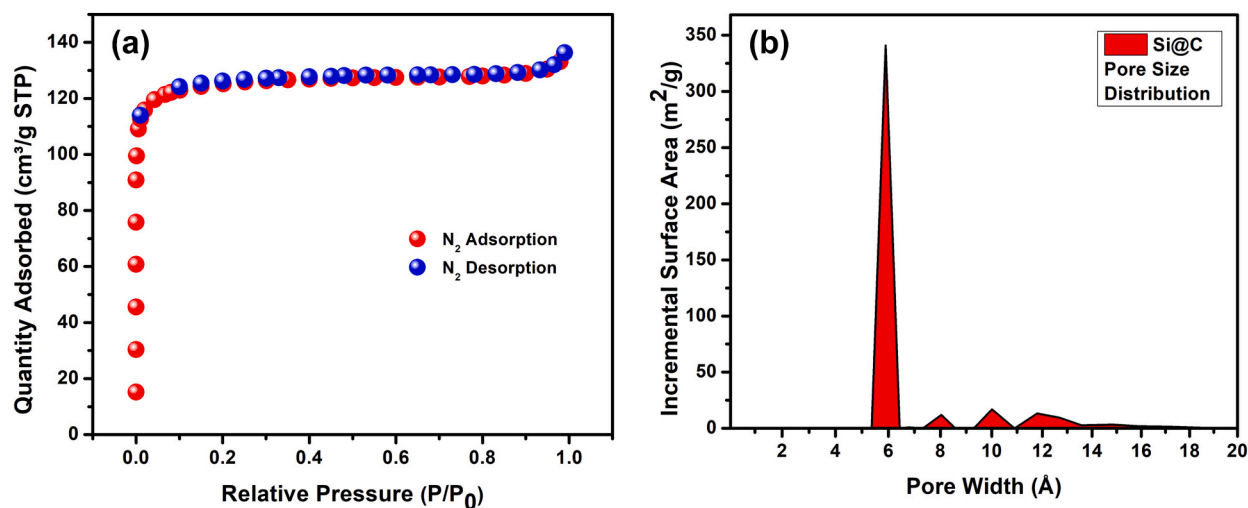


**Fig. 6.** (a) $N_2$ adsorption/desorption isotherms of Si@C, identifying a microporous carbon structure with the surface area of 400.1 m$^2$ g$^{-1}$; and (b) relative pore volume distribution of the carbon network showing a relatively uniform porous structure with its pore size concentrating at 5.90 Å.
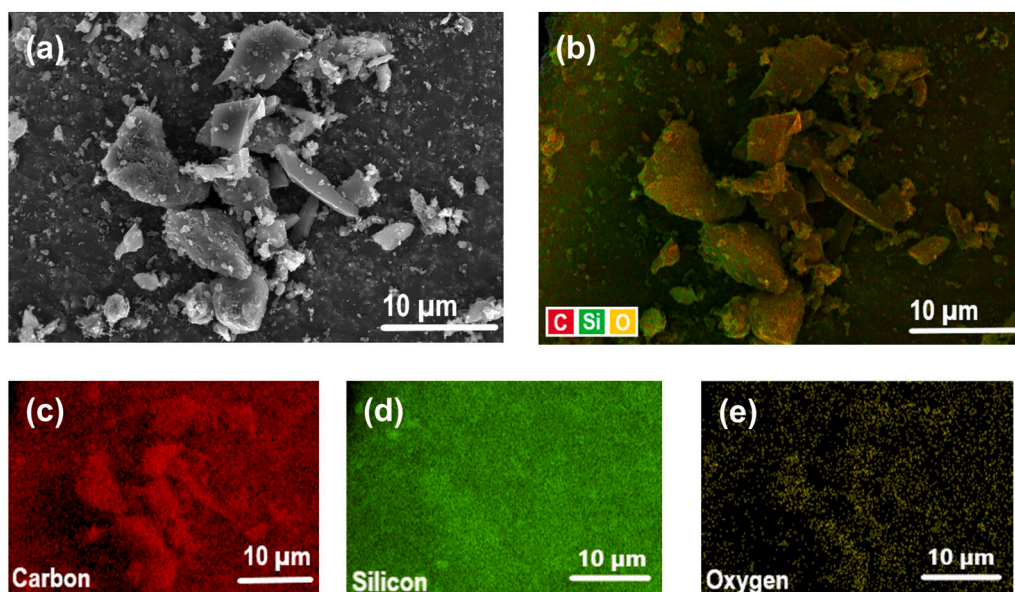
**Fig. 7.** (a) SEM image of Si@C magnified to 3500×, (b) EDS mapping of Si@C confirming the presence of C, Si, and O. EDS mapping of (c) Carbon, (d) Silicon, and (e) Oxygen elements. Ample and uniform distribution of Si loading was noticed.

conducted. GITT measurements conducted at various cycles are plotted in Fig. 8d. Typically for a LIB system, the internal resistance is mainly related to the electrolyte resistance, ionic mobility, and reactions at the electrode interfaces. The observed increase in internal resistance upon cycling can indicate: (1) an increase in electrolyte viscosity, (2) passivation of the electrolyte-electrode interfaces, and (3) degradation of the electrode's holding structures. From Fig. 8d, with prolonged cycling, an increase in the cell's internal resistance, which is represented by the height of each pulse interval, was observed. The total internal resistance mentioned here is the sum of various factors, including concentration polarization, activation polarization, charge transfer resistance, and proceeding reactions at the electrode-electrolyte interface. However, the ohmic resistance is the main contributor to this sharp rise. It should be noted that this ongoing increase of the overpotential associated with each interval is significantly larger for the charging cycles. Considering that the overall increase of electrolyte viscosity would have about the same impact during charge and discharge cycles, it can be implied that such a change is directly related to the electrode's structure. In this respect, the variation can indicate that the lithiation process becomes even more challenging as the cycling process goes deeper. Furthermore, the left shift of the GITT curves with an increase in cycle numbers indicates that charging takes more time than discharging at the same charge/discharge rate, and more Li-ions are advancing out of the structure than migrating inside. The Nyquist plots from impedance spectroscopy measurements are presented in Fig. 9. From the figure, while the plots' shapes at different cycle numbers are very similar, the extent of the semicircles grew much larger with continuous cycling. Besides forming a very thin SEI layer, Li-ions can undergo plating and stripping at the Li chip in the half cell. The increase in the extent of semicircles upon cycling can be due to progressive passivation of the Li surface and the formation of Li dendrites. Fig. 9b exhibits the Nyquist plot of the fully discharged state in which the Si@C electrode is fully lithiated. There are two main differences between the Nyquist plots of fully lithiated and completely delithiated states: (1) the magnitude of the peaks increases more rapidly for the fully discharged state, and (2) the curvature of the diffusion tail at the low-frequency region shows significant variance at different cycle numbers for the fully discharged state (see Fig. 9c). This dissimilarity, especially in composite materials, indicates the electrode's structural change, and researchers often neglect it. Wang et al. and Zhu et al.'s studies showed that diffusion length and

diffusion coefficient are the main parameters associated with the curvature of the diffusion tail [43,44]. Since the two criteria are directly related to the pore size, thickness, and crystalline structure of the electrodes, the curvature change is usually translated to structural variation of the material. This examination is crucial because it can relate capacity fading and resistance elevation to other factors rather than the degradation of the active materials. In a previous study, E. Casero et al. successfully distinguished the behavior of graphene oxide (GO) and reduced graphene by implementing EIS characterization and investigating the curvature of the diffusion tails [45]. In comparison to GO, rGO shows a similar semicircle behavior in the very low-frequency region (ion diffusion), but its magnitude is much smaller. Both rGO and GO possess finite diffusion length behavior, but rGO has a higher-ordered structure. Such behavior was not detected for aC and graphite.

According to our Raman Spectroscopy and XRD analyses, Si@C is mostly composed of aC, rGO, and Si. Our understanding is that Li alloying is initiated from the crystalline Si anchored onto rGO structures. As the cycling process went deeper, the ongoing activation of the mostly amorphous frame could change the pathway for Li-ions diffusion. Therefore, the nature of the reaction was altered, and the curvature of the diffusion tails was changed accordingly. This evaluation is in line with our GITT analysis, in which it was concluded that the number of Li-ions migrating out of the structure exceeds the number of ions moving into the structure. This consideration can only be valid if Li-ions are already trapped in the system in other forms. It is possible that with further activation of the mainly amorphous carbon network and the introduction of newly accessible pores and pathways, more trapped Li-ions could dealloy from the amorphous rGO-Si composition and participate in the reaction. A curvature slope analysis can further elucidate the aforementioned diffusion tail reasoning (Table S3). Fig. 9d shows the differential capacity versus the cell's voltage plot retrieved from the cycling data. Similar to CV analysis, the shape and location of the curves are accurately related to the anodic and cathodic reactions. From the graph, the anodic and cathodic curves are related to the lithiation and delithiation process of the amorphous Si. Further, the disappearance of the redox peaks can be due to the alteration of the active sites. This finding can further add to our previous EIS and GITT analyses. This conclusion was further intensified when disassembled batteries showed material detachment from the current collector, related to the electrode's material pulverization and structural
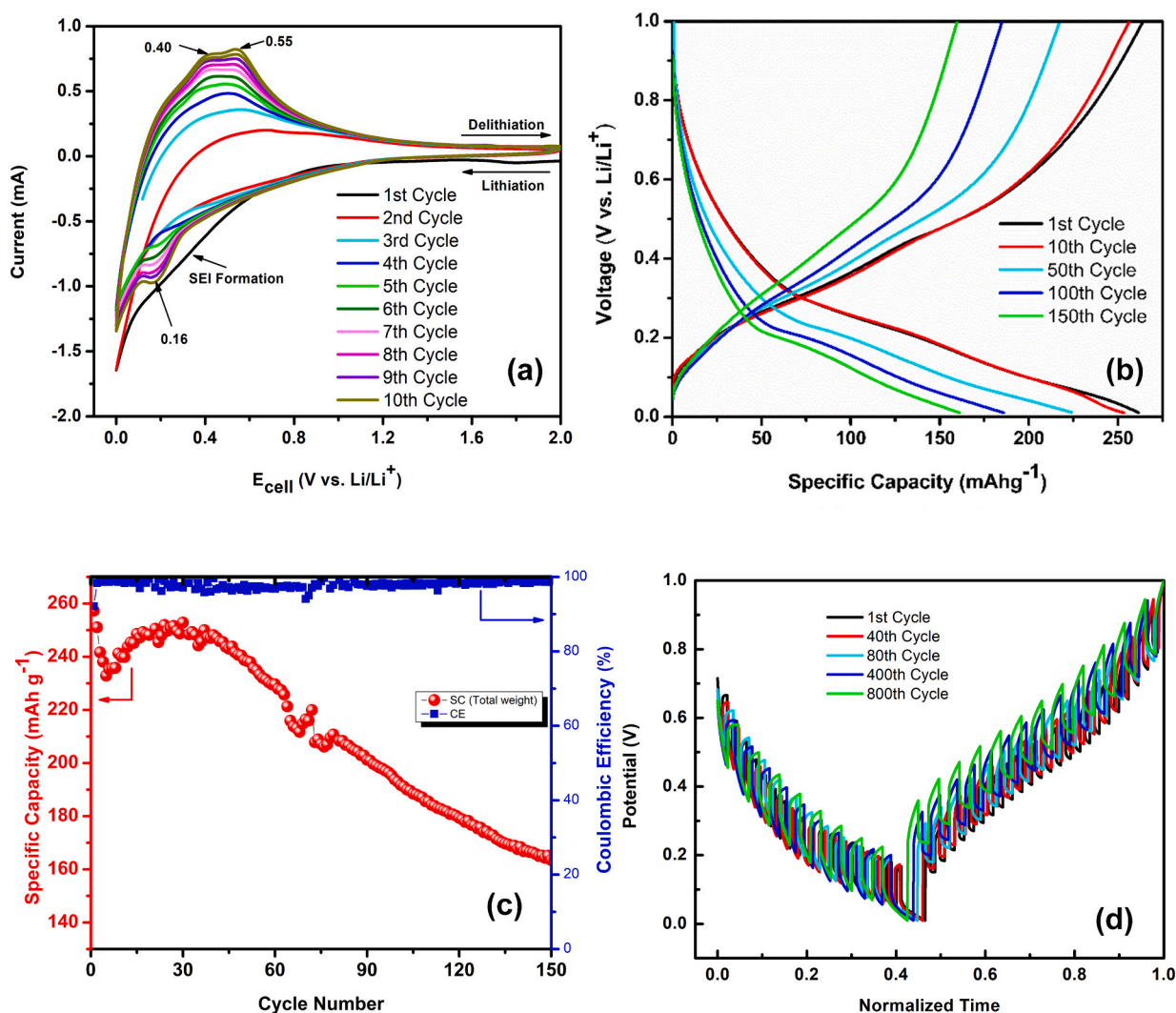
**Fig. 8.** (a) Cyclic voltammetry at a scan rate of 0.1 mV s$^{-1}$, exhibiting characteristic properties of amorphous Si and the presence of an activation process. (b) Charge/discharge voltage profiles of C—Si anode cycled at C/10, the results are in good agreement with our CV survey. (c) Cycling performance and Coulombic efficiency (CE) of C—Si anode; the device could retain 62 % of its initial capacity after 150 cycles; (d) GITT measurements at different cycles; the time axis is normalized to attain curve alignment.

transformation. For more in-depth qualitative research, the diffusion coefficient of the cells at fully discharged and charged states were studied based on the equation displayed below:

$$D = \frac{4}{\pi\tau}\left(\frac{V_m n_m}{S}\right)^2\left(\frac{\Delta E_s}{\Delta E_t}\right)^2$$

where $\tau$ is the duration of the current pulse; $V_m$ and $n_m$ refer to the electrodes' molar volume and the number of moles, respectively; and S is the electrode-electrolyte interface area. $\Delta E_s$ is the change in the steady-state voltage, and $\Delta E_t$ relates to the overall cell voltage after applying a current pulse in a single step GITT, eliminating the voltage change caused by the internal resistance [46]. In this study, the authors aim to observe the variation of the diffusion coefficient instead of actual value determination. In this respect, all the parameters except the changes in voltage were treated as constants, and therefore, variation of the diffusion coefficient only relies on the $\Delta E_s$ and $\Delta E_t$. Table 1 summarizes the calculated values along with the description of the observed changes.

## 3. Techno-economical analysis

Due to the increasingly severe repercussions of global pollution, the world targets a sustainable circular economy to mitigate the emerging problems. The traditional linear economy model usually does not consider recycling a priority. Therefore, the ultimate destination of the used/expired natural resources, such as plastics, is designed to go to waste. As mentioned previously, under the linear economy model, 5 to 12 million tons of plastic waste leak into the world's oceans every year, albeit unintentionally. The circular economy concept emphasizes "reuse, share, repair, refurbish, remanufacture, and recycle." The proposed upcycling PET waste method in this study provides a potential solution to mitigate global pollution problems and provides a great economical alternative for producing energy materials that fit the circular economy requirements of battery manufacturing for stationary storage applications. Since introducing the first commercialized Lithium-ion battery by SONY in 1991, graphite has been the most mature, trusted, and popular anode material. According to George Miller of Benchmark Mineral Intelligence [49], by 2030, the Lithium-ion energy storage industry will require about 3 million tons of graphite per year. Researchers expect the graphite demand from the battery sector to rise by 30 % annually, making it the hot commodity of the following years. Currently, raw graphite-related materials are seeing a yearly increase in tonnage pricing due to industrial mining limitations and insufficient resources. A recent marketing investigation report by
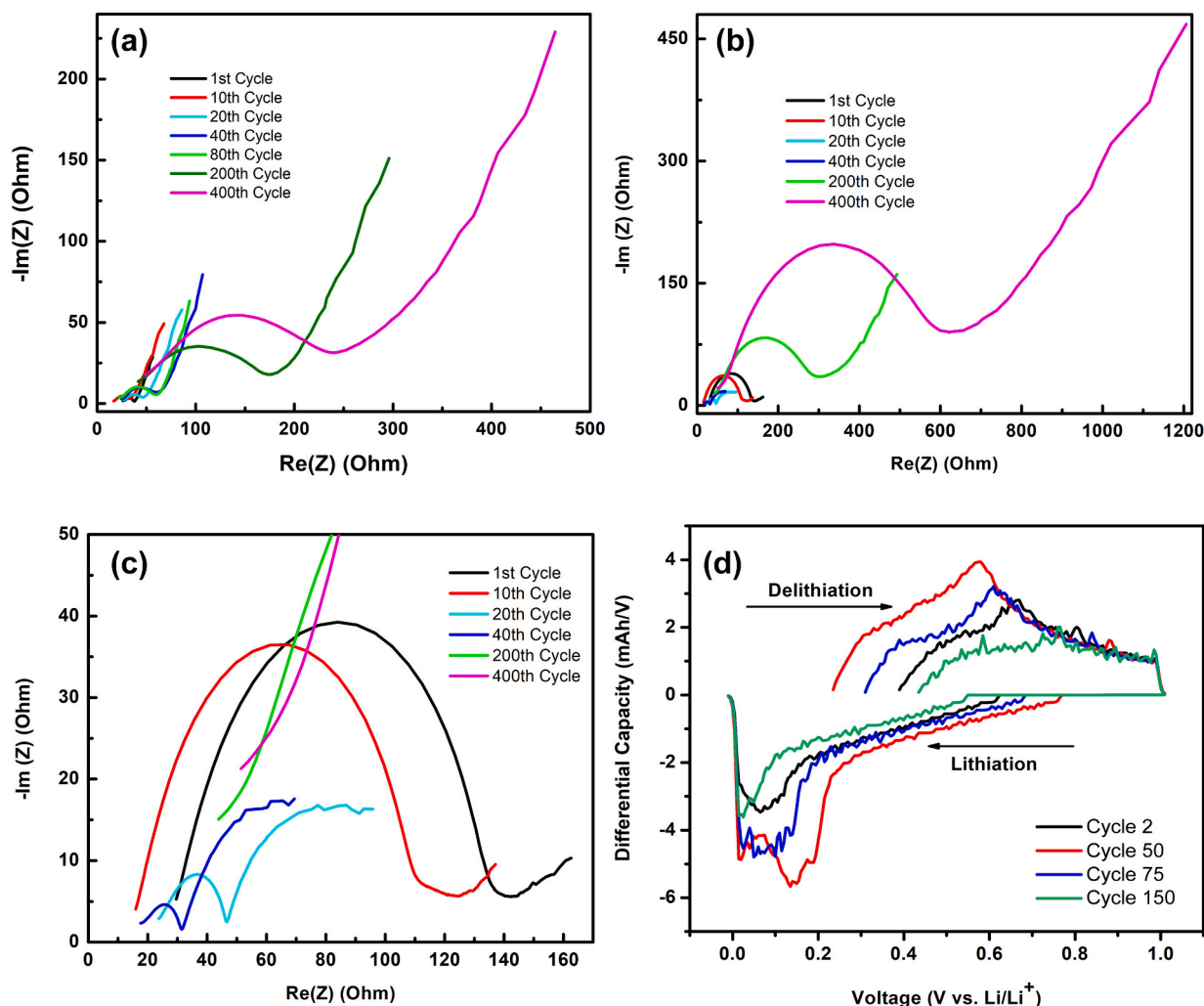
**Fig. 9.** EIS Nyquist plot of cycles at (a) fully charged state (Li electrode), and (b) fully discharged state (Si@C electrode); (c) magnified Nyquist plot of discharged state from 0 to 200 Hz frequency range, the rapid change in the curvature of the diffusion tail is suggestive of a change in the structure of the active sites; (d) Differential Capacity plots at different cycles calculated from C/5 cycling data, confirming a shift in the supported active sites' structure.

Statista GmbH indicated that carbon as a natural graphitic raw material (mined graphite) has a global reserve of approximately 320 million metric tons. Therefore, it is essential to find alternative approaches to producing energy storage materials; the ideal route is to make the process sustainable and circular [40–52].

Both natural and synthetic graphite materials are currently employed in manufacturing LIB anodes [53]. The price of high-quality and LIB-ready spherical graphite powder ranges from $8.00–$11.00 per kg (natural) to $20.00 per kg (synthetic). Due to increasing thermal and chemical processing costs, many battery manufacturers are transitioning to natural graphite [54]. Industrial LIB anode manufacturing based on natural graphite usually consists of (1) mining the raw material, which is calcined coke or flake graphite, (2) crushing and grinding processing, (3) chemical purification, and (4) baking or calcination in large batch furnaces (with temperatures at 1000–1300 °C, up to several weeks of thermal processing time).

This article targets the development of PET waste-derived carbon anode to manufacture ultra-low-cost LIBs for grid-level stationary energy storage applications. Note that PET waste, as the starting raw material for anode manufacturing, is far cheaper than natural graphite flakes, at an average of $0.19 per kg [55]. The overall processing steps for waste PET include (1) shredding and/or grinding, (2) chemical dissolution (TFA and DCM with nearly 100 % yield), (3) electrospinning to obtain nanofibers (high surface area), (4) thermal processing for carbonization (furnace processing time - up to 10 h, at 200–800 °C). The electrospinning step provides the means for obtaining a consistently high surface area material before the thermal processing, enabling an increase in surface reaction rates and effective carbonization. Over the past 50 years, large-scale electrospinning processing has seen significant advances in equipment development and has become very cost-effective. Their applications include but are not limited to filtration applications, such as manufacturing masks for the COVID-19 pandemic; wound dressing and sutures for a wide range of medical applications; tissue engineering; pharmaceuticals; composite materials; energy storage [56]. Around the world, several companies provide manufacturing scale electrospinning equipment and services suitable for various product designs and continuous production. For example, an Inovenso PE3550 system, a mid-level industry-level spinner, can produce electrospun fabrics over 7 Mm² year⁻¹. The system can utilize up to 56 nozzles, various solution chemistries (feeding rate up to 250 ml h⁻¹), and electrospinning voltage up to 40 kV. The Inovenso SS1000 system, a larger scale spinner, can utilize different solution chemistries with feeding rates up to 2500 ml h⁻¹, electrospinning voltage up to 80 kV, and manufacture fabrics 1 m wide at a rate of up to 50 m min⁻¹ [57].

## 4. Conclusion

This article introduced a scalable and industrially mature method for

**Table 1**
Diffusion coefficient variation at different cycle numbers. The values were calculated based on the voltage change, and they do not represent actual values.

| Cycle Number | Fully charged (~80 %) | Fully discharged (0 %) | Comments |
|---|---|---|---|
| 1st | 0.26548 | 0.17866 | Stimulation of the active material initiated. |
| 40th | 0.42124 | 0.18598 | The increase in the diffusion behavior indicates the persistent activation of the material. |
| 80th | 0.38254 | 0.10790 | The significant change in the diffusion coefficient is due to a change in the electrode's supported active sites (from mainly rGO to mostly aC) [47,48]. |
| 400th | 0.27873 | 0.11262 | The notable decrease of the diffusion coefficient at the fully charged state can be due to the growth of the passivation layers and dendrites on the anodic electrode. The slight increase of the diffusion coefficient at the fully discharged state indicates the slow activation process of the aC due to its high surface area and relatively small pore size. |
| 700th | 0.36949 | 0.10614 | The change in the diffusion coefficient is related to the decomposition and reformation of dendrites and the passivation layers on the anodic electrode, along with persistent passivation occurring on the cathodic side. |

the fabrication of carbon and composite C—Si active anode materials utilizing PET plastic waste. Silicon nanoparticles were embedded in the electrode structure through a solution and an electrospinning process, enabling the si particles to embed within the porous carbon architecture. DFTB+ calculations demonstrate close interactions between PET molecules and SiNPs that could help with the homogeneous distribution of the particles within the solution and, subsequently, the fiber structure. Analytical characterization of the electrode material, including SEM, EDS, Raman, XRD, and BET analyses, revealed the existence of polycrystalline silicon surrounded by a carbon supporting frame consisting of aC and rGO. We explored electrochemical behavior and the root causes of the degradation mechanisms of the composite by implementing CV, GCPL, GITT, EIS, differential capacity, diffusion tail, and diffusion coefficient investigations. Our studies revealed the following: (1) the presence of an activation process and SEI layer construction, (2) an ongoing increase in the internal resistance of the composite material that was mainly linked to the structural change of the electrode, (3) identification of trapped Li-ions and alteration of the Li-ion diffusion pathway with further cycling, (4) initiation of the lithiation process at Si sites anchored to rGO, (5) modulation in the structure of supported active sites with continuous cycling and (6) composition of the carbon frame consisting of aC and rGO. Our failure analyses identified the structural deformation of the electrode due to massive volume changes to be the primary reason for the capacity decay and aging of the battery. Considering the economic advantages of our approach, business models estimate the market valuation for stationary battery storage to cross $140 billion by 2030. Meanwhile, high demand for raw battery materials has pushed the prices, resulting in an increase in LIB production cost. The ideal way to secure a steady supply chain is to find circular and sustainable alternatives to transfer waste materials into valuable products, such as energy storage. In comparison to conventional industrial graphite manufacturing, we find our proposed method of carbon anode production to be a low-cost and sustainable alternative suitable for grid-level stationary energy storage applications. In the real world, plastic waste management and initial separation of plastic types can reduce the

pre-treatment costs can facilitate the implementation of recycling strategies. Such an approach can further pave the way to opportunities for fabricating economical active electrode materials and carbon additives, establishing a sustainable pathway for upcycling plastic waste in a circular economy.

## 5. Methods

### 5.1. Fiber production & carbonization

Commercially available SiNPs (80 nm in diameter) were added to a homogeneous 10 wt% PET solution, which was prepared by the dissolution of PET waste (PurAqua water bottle) in a mixture of trifluoroacetic acid (TFA, Alfa Aesar, 99 %) and dichloromethane (DCM, Acros Organics, 99.9 %, extra dry). The solvents ratio was 70 wt% and 30 wt% for TFA and DCM, respectively. In order to obtain a homogeneous dispersion of SiNPs, the solution mixture was mechanically stirred for 24 h, followed by sonication for 1 h prior to electrospinning. For the electrospinning process (Inovenso NE300 system), the solution feeding rate was set to 720 μL h$^{-1}$, and the chamber humidity level was maintained at 40 %. The spinneret was set at 12 cm from the collector plate, and the provided voltage for Taylor cone formation was 19 kV. Electrospinning provides the initial large surface area of the nanofibers architecture and enables a highly efficient and effective carbonization process. The carbonization was carried out in a quartz tube furnace (MTI, OTF – 1200× multizone system). This part of the process was conducted in 2 steps in a mixture of argon (Ar) and hydrogen (H$_2$) gas atmosphere with mass flow controller settings of 50 SCCM and 200 SCCM at 760 Torr for H$_2$ and Ar, respectively. In the first step, to sustain the fibers' structure, the temperature was ramped to 220 °C with a heating rate of 5 °C min$^{-1}$ and maintained at this temperature for 2 h. Next, the temperature was increased to 750 °C with the same heating rate and was held at this set-point for an additional 2 h. Carbonized samples of Carbon and Si@C were gradually cooled down overnight, followed by ball-milling (MTI, MSK -SFM-1 machinery) at 200 rpm for 2 h to produce homogeneous particles. The purpose of the first heat stage, at 220 °C, is to introduce the fibers to the new environment and allow for reaching a stable and thermodynamically favorable structure before the carbonization step at 750 °C. This method was effective in producing more uniform carbon materials with better efficiency.

### 5.2. Materials characterization & cell assembly

Carbon and Si@PET samples were sputter-coated with a thin layer of platinum for 30 s before the SEM measurements. Imaging and EDS measurements were carried out utilizing a ThermoFisher Scientific, NNS450 SEM with In-lens SE/BSE detector (TLD). Structural variations and composition of the Carbon, Si@PET, and Si@C were investigated using Raman spectroscopy via a Dilor XY Laser Raman system with an imaging microscope (532 nm Ar ion laser). XRD measurements were conducted using a PANalytical Empyrean series 2 system with 2θ linearity equal to or better than ±0.01°. BET analysis was carried out using a Micromeritics ASAP 2020 volumetric instrument. For N$_2$ isotherm sorption, the Si@C sample was firstly activated by evacuation ($10^{-3}$ Torr) at 200 °C for 12 h to remove water and gas. The Si concentration was determined using Thermogravimetric Analysis based on the stoichiometric ratio of SiO$_2$ (TGA, Mettler Toledo system, Fig. S1). With a heating rate of 30 °C min$^{-1}$, TGA was conducted from 25 to 850 °C using dry air (ultra-zero grade, Airgas) at 50 mL min$^{-1}$ as the feeding gas, completed over a 3-h isothermal step at 850 °C to ensure complete silicon oxidation. To produce carbon anodes, we mixed P750 with polyvinylidene fluoride (PVDF) with a ratio of 85:15 wt%, respectively. After adding N-Methyl-2-Pyrrolidone (NMP), we mechanically mixed the slurry for 24 h, followed by casting and drying at 100 °C overnight. An electrolyte solution of 1.0 M lithium hexafluorophosphate (LiPF$_6$) in a mixture of ethylene carbonate (EC) solvent and fluoroethylene

carbonate (FEC) additive with a ratio of 1:1 (*v*/*v*) was used. For Si anode electrode preparation, Si@C was mixed with polyacrylic acid (PAA) and carbon black with a ratio of 80:10:10 wt%, respectively. After adding NMP, the slurry was mechanically stirred for 24 h to obtain the desired viscosity and uniformity suitable for casting. Afterward, the slurry was cast on copper foil using a doctor blade system and dried overnight at 100 °C. Then the casted slurry was calendared to a thickness of ~0.2 mm prior to punching and assembly in a coin-type cell (CR2032, MTI). Final Si loading was around 0.51 mg cm$^{-2}$ for our cells. An electrolyte solution of 1.0 M lLiPF$_6$ in a mixture of EC and dimethyl carbonate (DMC) solvents with a ratio of 1:1 (v/v) was used. We performed our half-cell assemblies in an Ar-filled glovebox with H$_2$O and O$_2$ levels below 1 ppm. Pure lithium (Li) metal chip was employed as the counter electrode.

### 5.3. Electrochemical measurements

A Bio-Logic testing platform with BCS 810 modules was utilized in conducting the electrochemical measurements. CV was conducted at a scan rate of 0.1 mV s$^{-1}$ from 0 to 2 V. GCPL measurements under constant current (CC) cycling was performed within the potential window of 0–1 V. The cells were conditioned for four cycles at a CC of 71.44 mA g$^{-1}$ (at C/50) before cycling with a CC of 357.2 mA g$^{-1}$ (at C/10). EIS measurements were conducted every 10 cycles with a 10 mV AC perturbation signal. To minimize the electrodes' influence on another we performed the EIS measurements at fully charged and fully discharged states, within the range of 10 mHz to 10 kHz. GITT measurements were conducted from 0.01 to 1 V every 40 cycles; the applied current was set to 357.2 mA g$^{-1}$, with a 10-min rest interval.

### 5.4. Computational methods

Computations were performed using the DFTB+ code [58] with the pbc/pbc-0-3 [59–62] and ob2/ob2-1-1/base [63] sets of Slater-Koster parameters to investigate the structural and binding properties of interactions between PET molecules and SiNPs. The initial structures of SiNPs with different sizes ranging from 0.7 to 1.6 nm are shown in Fig. S2. The SiNPs were constructed using $30 \times 30 \times 30$ supercells based on the diamond cubic crystal structure (corresponding to the Fd-3 m space group). Spherical SiNPs were carved out of these bulk supercells for the computations. The radii of the nanoparticles were set to desired values, and only atoms within the sphere were considered, whereas those outside the sphere were removed.

### CRediT authorship contribution statement

AM, MO, and CSO designed and discussed all the experiments. AM conducted the materials synthesis and cell construction. AM, BD, and TZ performed the analytical characterization and galvanostatic intermittent titration technique (GITT), galvanostatic cycling (GC), cyclic voltammetry (CV), and electrochemical impedance spectroscopy (EIS) measurements. MK conducted the Density Functional Based Tight Binding (DFTB+) and energy minimization computational work. MO and CSO managed the research team. All authors reviewed the manuscript.

### Declaration of competing interest

The authors declare that they have no competing interests.

### Data availability

Data will be made available on request.

### Acknowledgments

### Appendix A. Supplementary data

Supplementary data to this article can be found online at https://doi.org/10.1016/j.est.2022.106329.

### References

[1] S.B. Borrelle, J. Ringma, K.L. Law, C.C. Monnahan, L. Lebreton, A. McGivern, E. Murphy, J. Jambeck, G.H. Leonard, M.A. Hilleary, M. Eriksen, Predicted growth in plastic waste exceeds efforts to mitigate plastic pollution, Science 369 (2020) 1515–1518.

[2] L. Lebreton, A. Andrady, in: Future Scenarios of Global Plastic Waste Generation And Disposal 5, Palgrave Communications, 2019, pp. 1–11.

[3] R. Geyer, J.R. Jambeck, K.L. Law, Production, use, and fate of all plastics ever made, Sci. Adv. 3 (2017), e1700782.

[4] C.J. Rhodes, Plastic pollution and potential solutions, Sci. Prog. 101 (2018) 207–260.

[5] J.R. Jambeck, R. Geyer, C. Wilcox, T.R. Siegler, M. Perryman, A. Andrady, R. Narayan, K.L. Law, Plastic waste inputs from land into the ocean, Science 347 (2015) 768–771.

[6] R.C. Thompson, Sources, distribution, and fate of microscopic plastics in marine environments, in: The Handbook of Environmental Chemistry, 2016, pp. 121–133, https://doi.org/10.1007/698_2016_10.

[7] M. Niaounakis, Degradation of plastics in the marine environment, in: Management of Marine Plastic Debris 127–142, 2017, https://doi.org/10.1016/b978-0-323-44354-8.00003-3.

[8] M.W. Ryberg, A. Laurent, M. Hauschild, Mapping of global plastics value chain and plastics losses to the environment: with a particular focus on marine environment, 2018.

[9] C.S. Lam, S. Ramanathan, M. Carbery, K. Gray, A Comprehensive Analysis of Plastics and Microplastic Legislation Worldwide, Water Air Soil Pollut 229 (2018) 345.

[10] M. Shen, W. Huang, M. Chen, B. Song, G. Zeng, Y. Zhang, (Micro)plastic crisis: un-ignorable contribution to global greenhouse gas emissions and climate change, J. Clean. Prod. 254 (2020), 120138.

[11] S. Abalansa, B. El Mahrad, G.K. Vondolia, J. Icely, A. Newton, The marine plastic litter issue: a social-economic analysis, Sustain. Sci. Pract. Policy 12 (2020) 8677.

[12] E. Iacovidou, A.P.M. Velenturf, P. Purnell, Quality of resources: a typology for supporting transitions towards resource efficiency using the single-use plastic bottle as an example, Sci. Total Environ. 647 (2019) 441–448.

[13] K.E. Lorber, G. Kreindl, E. Erdin, H. Sarptas, Waste management options for biobased polymeric composites, in: 4th International Polymeric Composites Symposium, 2015, pp. 1–9.

[14] S. Kumar, A.K. Panda, R.K. Singh, A review on tertiary recycling of high-density polyethylene to fuel, Resour. Conserv. Recycl. 55 (2011) 893–910.

[15] P. Brachet, L.T. Høydal, E.L. Hinrichsen, F. Melum, Modification of mechanical properties of recycled polypropylene from post-consumer containers, Waste Manag. 28 (2008) 2456–2464.

[16] M. Raja, N. Angulakshmi, A. Manuel Stephan, Sisal-derived activated carbons for cost-effective lithium–sulfur batteries, RSC Adv. 6 (2016) 13772–13779.

[17] K. Lota, I. Acznik, A. Sierczynska, G. Lota, The capacitance properties of activated carbon obtained from chitosan as the electrode material for electrochemical capacitors, Mater. Lett. 173 (2016) 72–75.

[18] P. Sun, H. Lu, W. Zhang, H. Wu, S. Sun, X. Liu, Poly(ethylene terephthalate): rubbish could be low cost anode material of lithium ion battery, Solid State Ionics 317 (2018) 164–169.

[19] P. Półrolniczak, D. Kasprzak, J. Kaźmierczak-Raźna, M. Walkowiak, P. Nowicki, R. Pietrzak, Composite sulfur cathode for Li-S batteries comprising hierarchical carbon obtained from waste PET bottles, Synth. Met. 261 (2020), 116305.

[20] S. Ghosh, M.A. Makeev, Z. Qi, H. Wang, N.N. Rajput, S.K. Martha, V.G. Pol, Rapid upcycling of waste polyethylene terephthalate to energy storing disodium terephthalate flowers with DFT calculations, ACS Sustain. Chem. Eng. 8 (2020) 6252–6262.

[21] K.S. Kim, J.U. Hwang, J.S. Im, J.D. Lee, J.H. Kim, M.I. Kim, The effect of waste PET addition on PFO-based anode materials for improving the electric capacity in lithium-ion battery, Carbon Lett. 1–9 (2020).

[22] A. Mirjalili, B. Dong, P. Pena, C.S. Ozkan, M. Ozkan, Upcycling of polyethylene terephthalate plastic waste to microporous carbon structure for energy storage, Energy Storage (2020), https://doi.org/10.1002/est2.201.

[23] R. Héliou, J.L. Brebner, S. Roorda, Optical and structural properties of 6H–SiC implanted with silicon as a function of implantation dose and temperature, Nucl. Instrum. Methods Phys. Res., Sect. B 175–177 (2001) 268–273.

[24] C. Zhu, N. Tong, L. Song, G. Zhang, Investigation of Raman spectra of polyethylene terephthalate, in: International Symposium on Photonics and Optoelectronics2015, 2015, https://doi.org/10.1117/12.2205157.

[25] N. Tong, C.J. Zhu, L.X. Song, C.H. Zhang, G.Q. Zhang, Y.X. Zhang, Characteristics of Raman spectra of polyethylene terephthalate, Guang pu xue yu Guang pu fen xi= Guang pu 36 (2016) 114–118.

[26] F.S. Tehrani, Transformation from amorphous to nano-crystalline SiC thin films prepared by HWCVD technique without hydrogen dilution, Bull. Mater. Sci. 38 (2015) 1333–1338.

[27] Y. Gogotsi, G. Zhou, S.-S. Ku, S. Cetinkunt, Raman microspectroscopy analysis of pressure-induced metallization in scratching of silicon, Semicond. Sci. Technol. 16 (2001) 345.

[28] C. Meier, S. Lüttjohann, V.G. Kravets, H. Nienhaus, A. Lorke, H. Wiggers, Raman properties of silicon nanoparticles, Phys. E. 32 (2006) 155–158.

[29] Y. Huang, Y. Zeng, Z. Zhang, X. Guo, M. Liao, C. Shou, S. Huang, B. Yan, J. Ye, UV-Raman scattering of thin film Si with ultrathin silicon oxide tunnel contact for high efficiency crystal silicon solar cells, Sol. Energy Mater. Sol. Cells 192 (2019) 154–160.

[30] C. Sheng, Char structure characterised by Raman spectroscopy and its correlations with combustion reactivity, Fuel 86 (2007) 2316–2324.

[31] S. Thakur, N. Karak, Green reduction of graphene oxide by aqueous phytoextracts, Carbon 50 (2012) 5331–5339. N. Y.

[32] M.S. Dresselhaus, A. Jorio, M. Hofmann, G. Dresselhaus, R. Saito, Perspectives on carbon nanotubes and graphene Raman spectroscopy, Nano Lett. 10 (2010) 751–758.

[33] B.D. Ossonon, D. Bélanger, Synthesis and characterization of sulfophenyl-functionalized reduced graphene oxide sheets, RSC Adv. 7 (2017) 27224–27234.

[34] J. Font, J. Muntasell, E. Cesari, Poly (butylene terephthalate) poly (ethylene terephthalate) mixtures formed by ball milling, Mater. Res. Bull. 34 (1999) 157–165.

[35] D. Lamba, Wide-angle X-ray diffraction pattern, in: Encyclopedia of Membranes 1–2, 2014, https://doi.org/10.1007/978-3-642-40872-4_1099-1.

[36] A. Magasinski, P. Dixon, B. Hertzberg, A. Kvit, J. Ayala, G.J. Yushin, High-performance lithium-ion anodes using a hierarchical bottom-up approach, Nat. Mater. 9 (2010) 353–358.

[37] W. Li, Y. Tang, W. Kang, Z. Zhang, X. Yang, Y. Zhu, W. Zhang, C.S. Lee, Core-shell Si/C nanospheres embedded in bubble sheet-like carbon film with enhanced performance as lithium ion battery anodes, Small 11 (2015) 1345–1351.

[38] M. Green, E. Fielder, B. Scrosati, Structured silicon anodes for lithium battery applications. and Solid-State, 2003.

[39] U. Kasavajjula, C. Wang, A. John Appleby, Nano- and bulk-silicon-based insertion anodes for lithium-ion secondary cells, J. Power Sources 163 (2007) 1003–1039.

[40] J. Li, J.R. Dahn, An in-situ X-ray diffraction study of the reaction of Li with crystalline Si, J. Electrochem. Soc. 154 (2007) A156–A161.

[41] Y. Chen, X. Li, K. Park, J. Song, J. Hong, L. Zhou, Y.W. Mai, H. Huang, J. B. Goodenough, Hollow carbon-nanotube/carbon-nanofiber hybrid anodes for Li-ion batteries, J. Am. Chem. Soc. 135 (2013) 16280–16283.

[42] Ali Davoodabadi, Jianlin Li, Hui Zhou, David L. Wood III, Timothy J. Singler, Congrui Jin, Effect of calendering and temperature on electrolyte wetting in lithium-ion battery electrodes, J.Energy Storage 26 (2019), 101034.

[43] J.G. Zhu, Z.C. Sun, X.Z. Wei, H.F. Dai, A new electrochemical impedance spectroscopy model of a high-power lithium-ion battery, RSC Adv. 4 (2014) 29988–29998.

[44] C. Wang, A.J. Appleby, F.E. Little, Electrochemical impedance study of initial lithium ion intercalation into graphite powders, Electrochim. Acta 46 (2001) 1793–1813.

[45] NASA Technical Reports Server (NTRS). https://ntrs.nasa.gov/search.jsp?R=20 120016539.

[46] Y. Zhu, C. Wang, Galvanostatic intermittent titration technique for phase-transformation electrodes, J. Phys. Chem. C 114 (2010) 2830–2841.

[47] I. Jung, D.A. Field, N.J. Clark, Y. Zhu, D. Yang, R.D. Piner, S. Stankovich, D. A. Dikin, H. Geisler, C.A. Ventrice Jr., R.S. Ruoff, Reduction kinetics of graphene oxide determined by electrical transport measurements and temperature programmed desorption, J. Phys. Chem. C 113 (2009) 18480–18486.

[48] M. Wu, B. Xu, C. Ouyang, Physics of electron and lithium-ion transport in electrode materials for li-ion batteries, Chin.Phys.B 25 (2016), 018206.

[49] B. Priscila, Graphite Outlook 2021: demand from battery segment to grow, Graphite Investing News, January 11, 2021. https://investingnews.com/daily/res ource-investing/battery-metals-investing/graphite-investing/graphite-outlook/.

[50] S. Damm, Q. Zhou, Supply and demand of natural graphite - DERA, in: Rohstoffinformationen 43, 2020, 36 pp.; Berlin.

[51] Statista GmbH, Reserves of graphite worldwide. https://www.statista.com/statisti cs/1172356/global-graphite-reservers, 2021.

[52] Mineral commodity summaries, PDF available at, The United States Government Publishing Office, 2021. doi:10.3133/mcs2021, https://pubs.er.usgs.gov/ publication/mcs2021.

[53] Ming Shia, Changlei Song, Zige Tai, Kunyang Zou, Yue Duan, Xin Dai, Su. Junjie, Yuanzhen Chen, Yongning Liu, Coal-derived synthetic graphite with high specific capacity and excellent cyclic stability as anode material for lithium-ion batteries, Fuel 292 (2021), 120250, https://doi.org/10.1016/j.fuel.2021.120250.

[54] The graphite market. https://westwaterresources.net/minerals-portfolio/graphit e-market/, 2021.

[55] Plastics recycling update. https://resource-recycling.com/plastics/2021/02/17/pr ices-for-post-consumer-plastic-bales-continue-to-rise/, 2021.

[56] Jiajia Xue, Tong Wu, Yunqian Dai, Younan Xia, Electrospinning and electrospun nanofibers: methods, materials, and applications, Chem. Rev. 119 (8) (2019) 5298–5415, https://doi.org/10.1021/acs.chemrev.8b00593.

[57] Inovenso Incorporated, PDF available at, https://www.inovenso.com/product/, 2022. doi:10.3133/mcs2021.

[58] https://eia-international.org/wp-content/uploads/2022-EIA-Report-Connecting-th e-Dots-SPREADS.pdf.

[59] B. Aradi, B. Hourahine, T. Frauenheim, DFTB+, a sparse matrix-based implementation of the DFTB method, J. Phys. Chem. A 111 (2007) 5678–5684.

[60] E. Rauls, J. Elsner, R. Gutierrez, T. Frauenheim, Stoichiometric and non-stoichiometric (101¯0) and (112¯0) surfaces in 2H–SiC: a theoretical study, Solid State Commun. 111 (1999) 459–464.

[61] C. Köhler, Z. Hajnal, P. Deák, T. Frauenheim, S. Suhai, Theoretical investigation of carbon defects and diffusion in α-quartz, Phys. Rev. B: Condens. Matter Mater. Phys. 64 (2001), 085333.

[62] A. Sieck, T. Frauenheim, K.A. Jackson, Shape transition of medium-sized neutral silicon clusters, Phys. Status Solidi 240 (2003) 537–548.

[63] V.Q. Vuong, et al., Parametrization and benchmark of long-range corrected DFTB2 for organic molecules, J. Chem. Theory Comput. 14 (2018) 115–125.